A Strong Underwater Soft Manipulator With Planarly-Bundled Actuators and Accurate Position Control

Kailuan Tang, Chenghua Lu, Yishan Chen, Yin Xiao, Shijian Wu, Shaowu Tang, Hexiang Wang, Binbin Zhang, Zhong Shen, Juan Yi, Sicong Liu, *Member, IEEE*, and Zheng Wang, *Senior Member, IEEE*

***Abstract*—Soft robotic manipulators have inherent advantages in underwater applications, as they generate motion by deforming seamless muscles rather than having rotational joints or sliding cylinders, as well as having excellent passive adaptability. However, limited by insufficient structural stiffness, achieving high payload and positioning accuracy remains challenging in existing soft manipulator designs. In this work, we propose an innovative approach to underwater soft manipulator design: 1) by constraining high-power optimized actuators with densely spaced lateral supporting plates, we could significantly enhance structural stiffness as well as improve the model accuracy drastically; 2) compaired with a novel flow-controllable open-circuit hydraulic actuation, we could keep the manipulator smoothly operated and depth-compensation-free; 3) in result, the manipulator could be modelled kinematically in a simplified way for position control. The entire workflow from mechanical design to actuation and control is presented. A prototype soft manipulator was developed to validate the proposed design experimentally.**

***Index Terms*—Soft robotics, underwater manipulator, hydraulic control system, kinematics.**

Manuscript received 22 April 2023; accepted 4 September 2023. Date of publication 27 September 2023; date of current version 9 October 2023. This letter was recommended for publication by Associate Editor F. Renda and Editor C. Laschi upon evaluation of the reviewers' comments. This work was supported in part by the NSFC under Grants 51975268 and 52105021, in part by Shenzhen Science, Tech. & Innovation Commission under Grants RCBS20210609104446099, JCYJ20220530114615034, and JCYJ20220818100417038, and in part by Guangdong Basic and Applied Basic Research Foundation under Grant 2021A1515110658. *(Corresponding author: Zheng Wang.)*

Kailuan Tang is with the School of Mechatronics Engineering, Harbin Institute of Technology, Harbin 150001, China, also with the Southern University of Science and Technology, Shenzhen 518055, China, and also with the Guangdong Provincial Key Laboratory of Human Augmentation and Rehabilitation Robotics in Universities, Southern University of Science and Technology, Shenzhen 518055, China (e-mail: tangkl@mail.sustech.edu.cn).

Chenghua Lu, Yishan Chen, Yin Xiao, Shijian Wu, Shaowu Tang, and Binbin Zhang are with the Southern University of Science and Technology, Shenzhen 518055, China (e-mail: ucas.luchenghua@gmail.com; 11930357@mail.sustech.edu.cn; 11612834@mail.sustech.edu.cn; 12132305@mail.sustech.edu.cn; 12232306@mail.sustech.edu.cn; zhangbb@mail.sustech.edu.cn).

Hexiang Wang is with the School of Mechatronics Engineering, Harbin Institute of Technology, Harbin 150001, China, and also with the Guangdong Provincial Key Laboratory of Human Augmentation and Rehabilitation Robotics in Universities, Southern University of Science and Technology, Shenzhen 518055, China (e-mail: hwan9789@uni.sydney.edu.au).

Zhong Shen is with the Department of Mechanical Engineering, The University of Hong Kong, Hong Kong (e-mail: shenzhong1911@gmail.com).

Juan Yi, Sicong Liu, and Zheng Wang are with the Southern University of Science and Technology, Shenzhen 518055, China, and also with the Guangdong Provincial Key Laboratory of Human Augmentation and Rehabilitation Robotics in Universities, Southern University of Science and Technology, Shenzhen 518055, China (e-mail: yij3@sustech.edu.cn; liusc@sustech.edu.cn; wangz@sustech.edu.cn).

This letter has supplementary downloadable material available at https://doi.org/10.1109/LRA.2023.3320017, provided by the authors.

Digital Object Identifier 10.1109/LRA.2023.3320017

I. Introduction

UNDERWATER (UW) manipulation and sampling are challenging tasks in marine exploration [1], [2], where remotely operated vehicles (ROVs) are often employed to replace human divers to reduce life risks [1], [3]. However, with manipulation being the core of such tasks, UW manipulators, with their sizes, weights, payloads, and accuracies, are essential factors largely determining the operation capabilities of such ROV platforms [4], [5], [6]. Dominating conventional rigid UW manipulators achieve high payload and control accuracy with generally bulky and heavy bodies and high-power hydraulic, motor-based control [5], [7] or cable-driven rigid manipulator [8] lacking sufficient compliance when handling fragile or flexible UW objects [9], [10].

Trending soft UW manipulators excel in this regard with their inherent, material-induced flexibility, passive adaptability and seamless nature [11], [12], [13], [14], at a price of having moderate payloads and accuracies due to limited structural rigidity insufficient against UW disturbances [7], [15]. Soft-rigid hybrid (SRH) design appears to be a promising approach, using soft muscles to drive rigid kinematic components, achieving substantial increases (by orders of magnitudes) in both payload and accuracy in grippers and manipulators [2], while also benefiting from the soft robot's inherent compliance and water-proofing advantages [14], [15], [16]. While, SRH designs are also restricted by the added rigid kinematic structures, e.g., joints and hinges, offering compliance only in selected directions, while having similar waterproofing [16], [17] and working depth compensation problems [18], [19] seen in rigid UW robots.

Soft continuum manipulator could be an appropriate design with multiple DoFs and omnidirectionally compliance, while granting sufficient structural stiffness and payload capability [20]. We have revealed that the absence of spine-like rigid linkages [21] as central support requires careful consideration of the axial spacing between two adjacent supporting plates in relation to the radius of the soft muscle actuators [22]. Without this dimensional constraint, the manipulator segment is prone to significant buckling under axial compressional loading [20], [23]. Additionally, the constraint is less significant with lateral spacing of the soft actuators, as reported in the literature regarding contractile type of manipulators [24], [25].

In this work, we propose a novel high-performance UW soft manipulator system, to achieve strong, dexterous, accurate UW operations without depth compensation while remaining compliant, compact and lightweight. The main novelties and contributions are:

1) Mechanical design: we have shown that using densely-bundled soft-actuators in continuum manipulators could achieve bidirectional actuation with high strength; and adding intermediate structural support between adjacent supporting plates could significantly reduce lateral and shear buckling, while substantially improve modeling accuracy for actuation and control.
2) Actuation and control: a Flow-controllable Open-Circulation (FOC) compact hydraulic actuation system was proposed. Based on the principle of connected vessels and power-controllable gear pumps, the system is featured with smooth and depth-compensation free pressure control.
3) Base on the above two aspects, we proposed the design of a novel dual-segment hydraulic-enhanced origami (DSHO) soft actuator incorporating the over-constrain design method, and an omnidirectionally compliant, Planarly-bundled and Overly-Constrained (PBOC) soft-robotic joint constructed with DSHO actuators, which exhibited prominent compliance with Constant Curvature Assumption (CCA) [26] and consequently accurate position and pressure tracking with primitive semi-open-loop control utilized in our FOC system.

The rest of this article is organized as follows. The concept of the PBOC design is presented in Section II. Modeling of the DSHO actuator and the PBOC manipulator joint and control method is presented in Section III. Section IV presents experiment validations of the DSHO actuator, joint and manipulator. And Section V makes a conclusion.

II. System Concept and Design

A. System Concept

Distinctive from the joints based on contractile type actuators, such as McKibben actuators, where the relationship between actuator length, L and inter-actuator spacing, D, is crucial design parameters (Fig. 1(a)) [24], [25], those based on densely-bundled soft muscle actuators possess a bidirectional actuation capability instead of contraction only (Fig. 1(a2) (b2)) and diameters not neglectable, which makes the relationship between actuator length, L and actuator diameter, d, is more significant (Fig. 1(a1)) [22]. However, both of these two types of joints may suffer from buckling [20] while being loaded axially (Fig. 1(a3) (b3)) or shearing while being loaded laterally (Fig. 1(a4)(b4)). In this work, to strength the structural stiffness of a joint based on densely-bundled soft muscle actuators, over-constrain design method was excuted by spliting the actuator length, L, into two fractions with a supporting plate (Fig. 1(c1)). In Section IV-B, this modification was proven to be able to restrict buckling even if a heavy axial payload is exerted (Fig. 1(c3)), and result in bending instead of shearing, that is, the actuator axis will be approximately arc-shaped, under lateral payload (Fig. 1(c4)). Equiped with the supporting plate, a joint obtained largely lifted accordance with CCA, enabling the development an effective kinematic model.

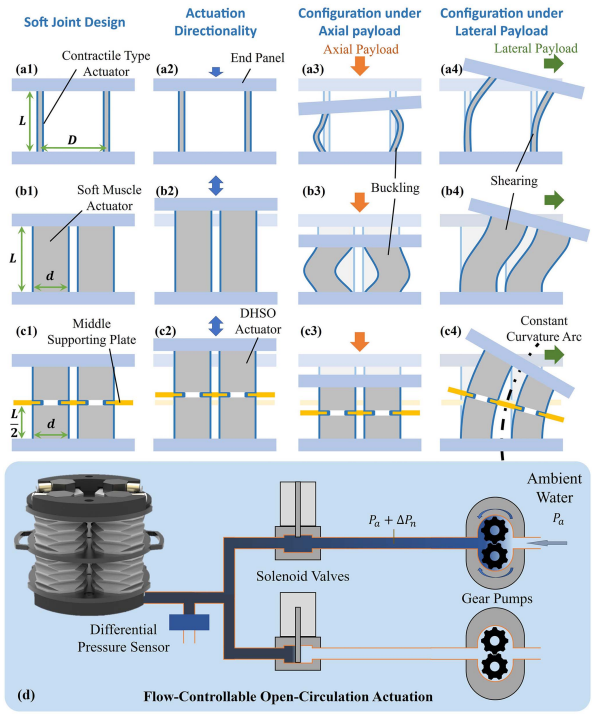

Fig. 1. Concept of the proposed PBOC design. (a1), (b1), and (c1) Natural state of contractile type muscle based joint, densely-bundled soft muscle based joint and PBOC joint design with DSHO actuator. (a2), (b2), and (c2) Actuation directionality of the three types of joints. (a3), (b3), and (c3) Deformation with axial load of the three designs. (a4), (b4), and (c4) Deformation with lateral load of the three designs. (d) The design concept and principle of the FOC actuation system.

The flow-controllable and depth-compensation free characteristics were facilitated by the FOC compact hydraulic actuation system (Fig. 1(d)), which comprises a fully open-circulation framework with introducing in-situ water inlet & outlet by connecting one side of the pipeline to the environment, therefore the ambient water pressure is balanced out and so the pumps are only required to generate pressure increment over the ambient pressure to drive the actuators, even if the depth changes. Different from our previous work [2], the proposed FOC system realizes multipath-independent pressure control with unique power-controllable gear pumps, paving the way for spatial kinematic control and smooth pressure tracking, which is validated in Section IV-E.

Integrating the over-constrain design and the FOC actuation system, the manipulator system was experimentally validated in Section IV-D to be competent to achieve accuracy trajectory tracking underwater.

B. Design of Actuator and Joint

1) The Design of DSHO Actuator: Based on our preliminary exploration of soft origami actuators [27], [28], [29], we presented a DSHO actuator with optimal materials and geometry. The thermoplastic polyurethane (TPU) soft body of the DSHO actuator was designed with a neck to adapt the supporting plate. The aluminum alloy end caps with tube connector were adhered to the soft body with superglue for sealing. The overview of

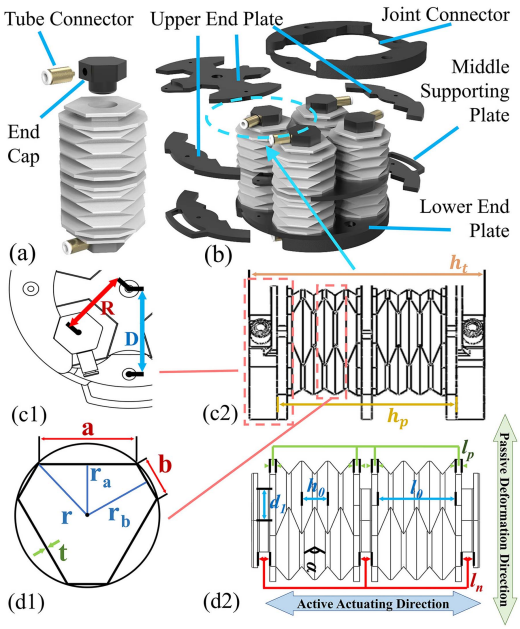

Fig. 2. Exploded drawing of the DSHO actuator (a), and the PBOC joint (b). (c1) The top view, and the side view (c2) of the PBOC joint. The top view (d1), and the side view (d2) of the DSHO actuator.

TABLE I
GEOMETRY OF THE ACTUATOR AND THE JOINT

l_0	Initial height of the folding segment	25.8 mm
h_0	Initial height between two folding peaks	8.6 mm
t	Thickness of the actuator	2 mm
r_1	Radius of actuator neck	12 mm
α	Dihedral angle of two trapezoid facets	73.4°
l_n	Length of actuator neck	4 mm
l_p	Thickness of folding segments' end plane	2 mm
r	Cross-sectional sizes of the actuator	23.71 mm
r_a		22.6 mm
r_b		17.51 mm
D	Radius of the joint end panel	122 mm
R	Assembling radius of actuators	35 mm
h_t	Total height of the PBOC joint	93.6 mm
h_p	Upper-lower end plate distance	71.6 mm

DSHO actuator design is shown in Fig. 2(a). The geometrical parameters could be found in Fig. 2(d1) (d2), and Table I.

2) The Design of the PBOC Joint: A joint based on the PBOC design was proposed with geometric parameters shown in Fig. 2(c1) (c2), and Table I. The assembly is shown in Fig. 2(b). Three aluminum alloy plates in the joint made 4 adjacent paralleled DSHO actuators mutually restraint in the radial direction of the joint. Moreover, joints could be connected serially with nylon joint connectors.

3) The FOC Actuation System: The FOC actuation system was designed to implement channel-independent pressure regulation for the robotic system. The system architecture is illustrated in Fig. 3(a) and the constructed system is shown in Fig. 3(b) with two components:

Electronic control layer: In Fig. 3(b) 3(B), the pressure information from the relative hydraulic pressure sensors (24PCDFA6D, Honeywell) is sampled by the external ADC

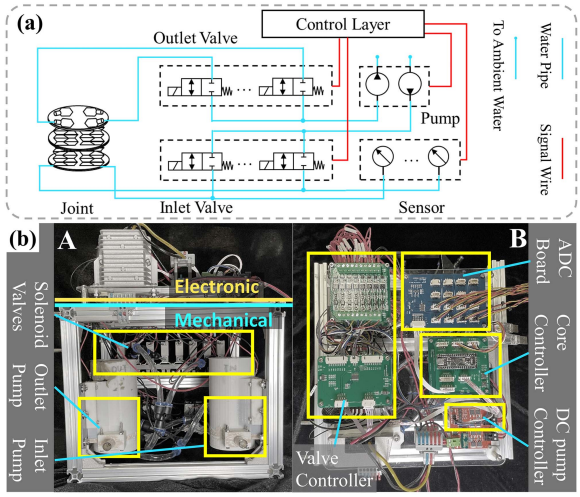

Fig. 3. (a) Architecture of the FOC actuation system. (b) (A) Lateral view, and top view (B) of the FOC actuation system prototype.

board (AD7490, ADI) and then sent to the core controller (STM32F411CEU6, STM), whose commands are conducted by the valve controller (PCA9539, NXP and CAO8A-P, Macrowis) and the DC pump controller (160D, ELECFANS).

Mechanical actuation layer: Pressures regulation in the DSHO actuators is undertaken by a group of solenoid valves (VDW12EA, SMC) and gear pumps (ZC-530, LAZC) jointly (see in Fig. 3(b)(A)). All of electronics had been encapsulated with epoxy resin for waterproofing. A detailed theoretical analysis of the control system is shown in III-C.

III. MODELING AND CONTROL

A. Modeling of the DSHO Actuator

The output force F_{total} of a DSHO actuator depends on the force generated by spring-like deformation ΔL and the force produced from the relative pressure P_m[27]:

$$F_{total} = F_d(\Delta L) + F_s(P_m). \tag{1}$$

According to the geometric parameters of DSHO actuator in Table I, the total length can be derived as

$$L = \frac{\pi D_e^2}{4K} P_m + 2l_p + l_n + 2l_0, \tag{2}$$

where D_e is the actuator effective diameter and K the stiffness coefficient, both of which could be determined experimentally. The model will be validated in IV-A and applied in IV-E.

B. Kinematics of the PBOC Joint

Following the constant curvature assumption (CCA) [26], a DSHO actuator tends to bend as an arc, as shown in Fig. 4(a)(b). We defined θ as the bending angle, i.e., the intersection angle of plane $O_2X_2Y_2$ and $O_1X_1Y_1$, κ as the curvature of l_j (virtual arc passes through the two planes' origins, O as the virtual center of l_j, and φ as intersection angle of $\overrightarrow{O_1X_1}$ and $\overrightarrow{O_1O}$ respectively in the configuration space. $\{l_1, l_2, l_3, l_4\}$ are the arc lengths of actuators and can be calculated from internal relative pressure $\{p_1, p_2, p_3, p_4\}$ with (2). The constraints of this model are defined as $l_j\kappa = 1$, $l_j = r\theta$, $l_j = (l_1 + l_2 + l_3 + l_4)/4$ and $l_1 + l_3 = l_2 + l_4$.

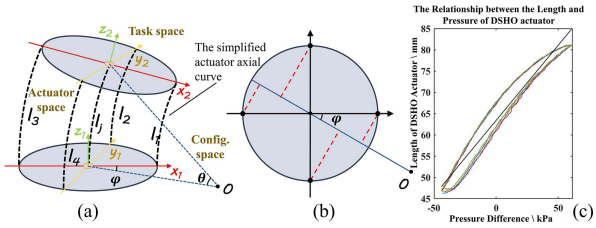

Fig. 4. Actuator and Joint Specification. (a) Simplified structural diagram and kinematics models of the joint. (b) Top view of (a). (c) Relationship between the length and the pressure of the DSHO actuator.

1) Forward Kinematics Model: Forward kinematics transforms lengths of the DSHO actuators $\{l_1, l_2, l_3, l_4\}$ to pose $\{x, y, z, raw, pitch, yaw\}$ of the endpoint of the joint. The arc parameters were derived as

$$\begin{cases} \varphi = arctan\left(l_4 - l_2, l_3 - l_1\right), \varphi \in [0, 2\pi], \\ \theta = \frac{\sqrt{(l_4-l_2)^2+(l_3-l_1)^2}}{2R}, \theta \in \left[0, \frac{\pi}{2}\right], \\ r = \frac{2l_jR}{\sqrt{(l_4-l_2)^2+(l_3-l_1)^2}}, r \in (0, +\infty). \end{cases} \tag{3}$$

Applying D-H method and considerating the deviation of the real fabricated joint from the ideal model, the transformation from the actuator space to the task space was given as the following equations:

$$\begin{matrix}\mathbf{2}\\\mathbf{1}\end{matrix}\boldsymbol{T} = \begin{bmatrix} c^2\varphi\left(c\theta-1\right)+1 & s\varphi c\varphi\left(c\theta-1\right) & c\varphi s\theta & rc\varphi\left(1-c\theta\right) \\ s\varphi c\varphi\left(c\theta-1\right) & s^2\varphi\left(c\theta-1\right)+1 & s\varphi s\theta & rs\varphi\left(1-c\theta\right) \\ -c\varphi s\theta & -s\varphi s\theta & c\varphi & rs\theta \\ 0 & 0 & 0 & 1 \end{bmatrix}, \tag{4}$$

$$\boldsymbol{X_{ideal}} = [x, y, z]^T = [rc\varphi\left(1-c\theta\right), rs\varphi\left(1-c\theta\right), rs\theta]^T, \tag{5}$$

$$\begin{aligned} \boldsymbol{X_{task}} &= \boldsymbol{X_{ideal}} + f\left(\boldsymbol{X_{ideal}}\right) \\ &= [x, y, z]^T + [a_x x^2 + b_x x + c_x, a_y y^2 + b_y y + c_y, a_z z^2 \\ &\quad + b_z z + c_z]^T, \end{aligned} \tag{6}$$

where $\begin{matrix}\mathbf{2}\\\mathbf{1}\end{matrix}\boldsymbol{T}$ is the transformation matrix from coordinate $O_1X_1Y_1Z_1$ to $O_2X_2Y_2Z_2$, $\boldsymbol{X_{ideal}}$ is the theorical translation of the endpoint, $\boldsymbol{X_{task}}$ is the endpoint position in task space with deviation compensation function $f(\boldsymbol{X_{ideal}})$ obtained by forward kinematic test experiment. This model will be validated experimentally in IV-D.

2) Inverse Kinematics Modeling: According to forward kinematics, the configuration parameters could be derived from (5): $\varphi = arctan(y_i/x_i)$, $\theta = 2arctan(\sqrt{x_i{}^2 + y_i{}^2}/2)$, and $r = z_i/sin\theta$, where $\{x_i, y_i, z_i\}$ $(z_i > 0)$ is the ideal endpoint position solvable with the desired position $\{x_d, y_d, z_d\}$ $(z_d > 0)$, and (6). Furthermore, using (3) and (5), we solve $\{l_1, l_2, l_3, l_4\}$ as

$$\begin{aligned} &[l_1, l_2, l_3, l_4]^T \\ &= \theta\left[r - Rcos\varphi, r - Rsin\varphi, r + Rcos\varphi, r + Rsin\varphi\right]. \end{aligned} \tag{7}$$

With the model of the DSHO actuator from section A, we can calculate target internal relative pressure $\{p_1, p_2, p_3, p_4\}$ of the DSHO actuators using the lengths result in (7). The result will be used and verified experimentally in IV-E.

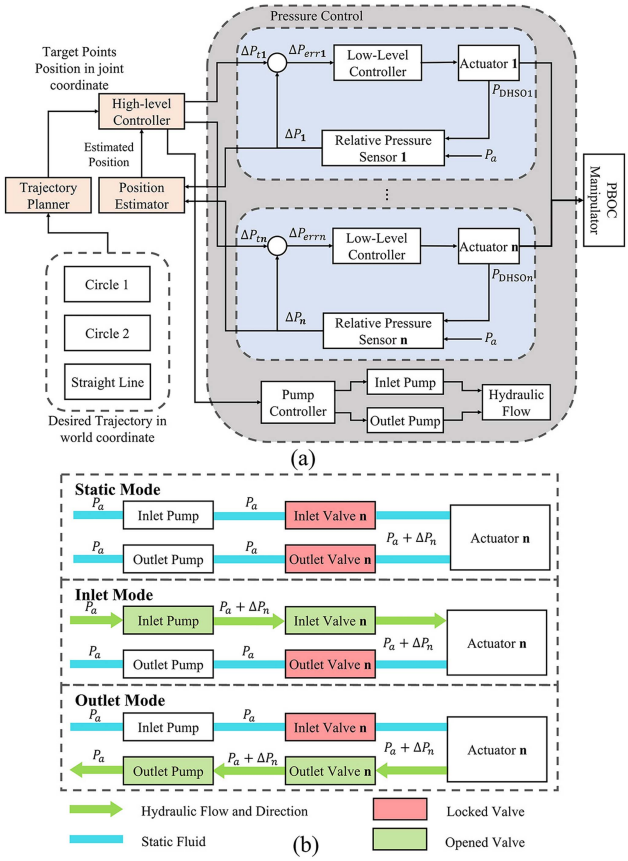

Fig. 5. (a) Total system control workflow. (b) Operation modes of the low-level controller. In static mode, neither inlet fluid nor outlet fluid is needed for the actuator. The system maintains pressure balance. In both inlet and outlet mode, the corresponding pump and valve are enabled, and fluid flows in the pipeline until the pressure in the actuator reaches ΔPn.

C. Control Methods

The position control architecture consists high-level (HL) position-control loop and low-level (LL) pressure-control loop (see in Fig. 5(a)). The HL controller estimates the PBOC joint position with ΔP_n from relative pressure sensors and computes required relative pressures ΔP_{tn} of a target position, where P_a is the ambient water pressure and P_{DSHOi} is the internal pressure of the i-th DSHO actuator.

Given ΔP_n from the HL controller, the LL controller regulates the relative pressure of each DSHO actuator channel independently in realtime with a binary control strategy with deadzones by operating pumps and valves. In the LL control strategy, three operation modes (see in Fig. 5(b)) are conducted depending on the magnitudes of ΔP_{err}. The hydraulic flows of pumps in the FOC system could be regulated by the HL controller, which is shown in Section IV-E.

Additionally, a trajectory planner was designed to control the PBOC manipulator along the desired path. A continuous trajectory can be discretized into a target position sequence transmitted to the HL controller. The position control and trajectory tracking will be validated in Section IV-D and E.

TABLE II
SUMMARY OF THE MANIPULATOR PERFORMANCE AND COMPARISON WITH OTHERS WORKS

Publications	This Work	[8]	[2]	[15]	[30]	[7]
Stiffness	Soft	Rigid	Soft-rigid hybrid	Soft	Soft-rigid hybrid	Rigid
Actuation System	Hydraulic	Cable	Hydraulic	compressed Air	compressed Air	Motor
Maximum Payload	559 N	44.1 N	15 N	-	19.6 N	245 N
Typical Position Control Accuracy	1.7 mm	1.02 mm, (0.07°)	1 mm	13.4 mm	1.5 mm	-
System Weight in Air	5.83 kg	24.75 kg	2.5 kg	-	3.5 kg	25 kg
Load-to-weight Ratio	9.78	0.182	0.612	-	0.5714	1
Working Range:	188 mm,(103.9%)		31.4 mm,(62.8%)	250 mm,(60.1%)		1550 mm,(165%)
X, Y, Z axis	188 mm,(103.9%)	-	31.4 mm,(62.8%)	260 mm,(62.5%)	-	-, (-)
(% of Length)	70 mm,(38.7%)		7.7 mm,(15.4%)	230 mm,(55.3%)		1000 mm,(106.5%)
Peak Power	50 W	-	34.4 W	-	-	25 W
DOFs	5	4	2	3	6	5
Maximum tested depth	60 m	-	4 m	10 m	-	300 m

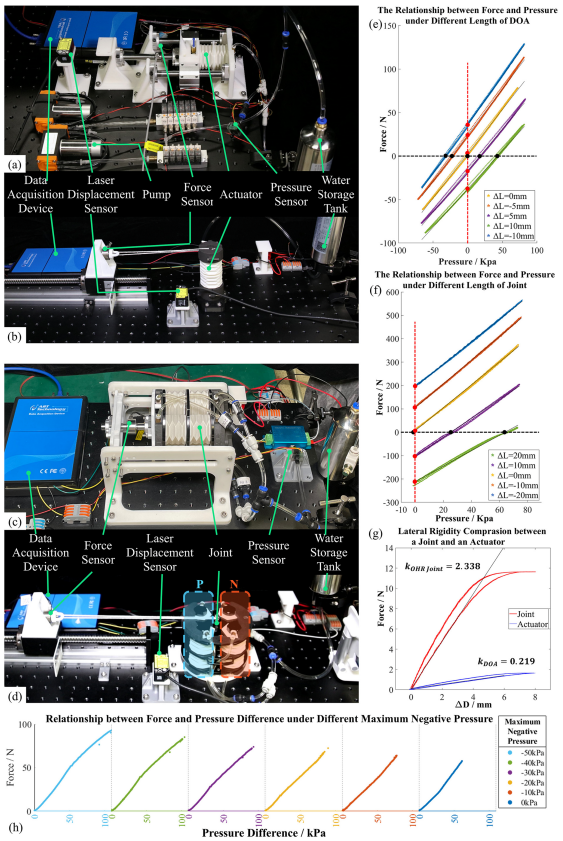

Fig. 6. (a) and (c) Force and length test device of the DSHO actuators and the PBOC joint. (b) and (d) Lateral stiffness test device of the actuators and the joint. The relationship between output force and internal pressure of (e) the actuators and (f) the joint. (g) Lateral rigidity comparison between the actuators and the joint. The two actuators in square N are negative group, the two in square P are positive group. (h) Relationship between force and pressure difference under different maximum negative pressure.

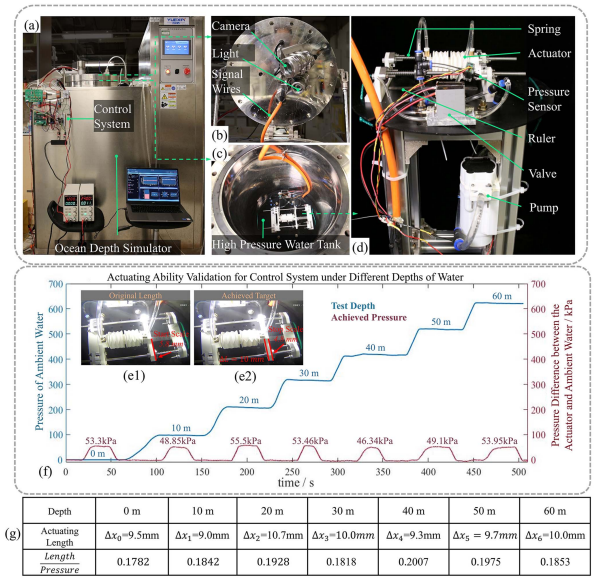

(g)

Depth	0 m	10 m	20 m	30 m	40 m	50 m	60 m
Actuating Length	Δx_0=9.5mm	Δx_1=9.0mm	Δx_2=10.7mm	Δx_3=10.0mm	Δx_4=9.3mm	Δx_5 = 9.7mm	Δx_6=10.0mm
$\frac{Length}{Pressure}$	0.1782	0.1842	0.1928	0.1818	0.2007	0.1975	0.1853

Fig. 7. (a) Total view of the test device, (b) cap of the ocean depth simulator tank, (c) the minimum actuation device placed in the tank, (d) minimum actuation device with a pump, two valves and a DSHO actuator, (e1) and (e2) show the original and actuated state of the DSHO actuator at 60 m depth in the ocean depth simulator tank, (f) the simulated ambient pressure curve and control results. Table (g) shows all tests' numerical results. The other test images at different depths are shown in the attached video.

IV. EXPERIMENT VALIDATIONS

A. Performance Test of the DSHO Actuator

1) Actuator Active Actuation Test: The actuation tests of DSHO actuator were conducted in the test platform (Fig. 6(a)). A laser displacement sensor (HG-C1200, Panasonic) measured the length of the DSHO actuator. An axial force sensor (AR-DN102, ARIZON) measured output force. A relative pressure sensor connected to the pipeline measured the relative internal pressure. The hydraulic pressure was exerted by regulating the air pressure in the half-filled water tank, with two air pumps and two solenoid valves.

The right side of the DSHO actuator was mounted on a fixed base and the left side was connected to a slider installed on two linear slideways. By fixing the slider, the relationship of internal pressure and output force of a DSHO actuator in 5 different fixed lengths was recorded and shown in Fig. 6(e). And the relationship of internal pressure and length with the actuator extending free was recorded and plotted in Fig. 4(c). The curve-fitting result shows the length-pressure model of the DSHO actuator is $L = 0.3532P_m + 63.41$. The D_e in (2) was obtained as 41.01 mm and the stiffness coefficient K as 3.74 N/mm in (2). Additionally, it was shown that the single

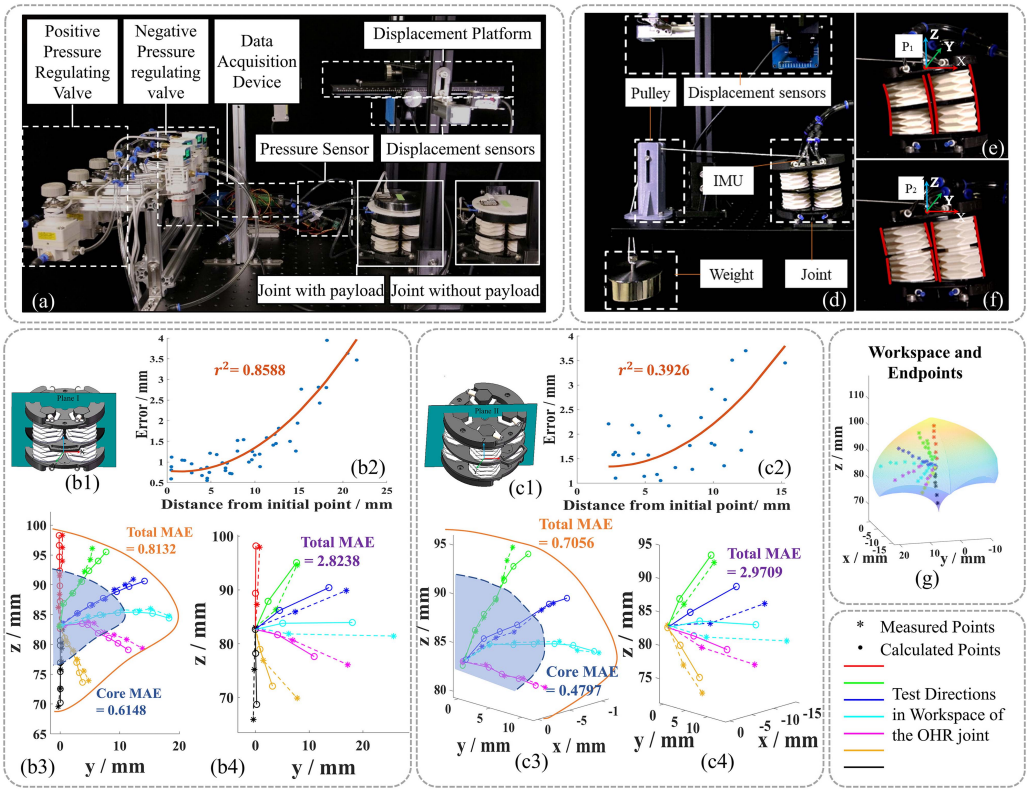

Fig. 8. (a) Forward kinematics testing device. The kinematic test plane I (b1) and plane II (c1). Relationships between position deviation and distance from the initial point and the polynomial-fitted curves without payload on plane I (b2) and plane II (c2). Calculated and measured endpoint positions without payload on plane I (b3) and plane II (c3) after deviation compensating with MAE values. Calculated and measured endpoint positions with payload on plane I (b4) and plane II (c4) with MAE values. (d) The disturbance test device. (e) The result of joint with the supporting plate when a lateral payload was applied. (f) The result of joint without the supporting plate when a lateral payload was applied. (g) The workspace and measured endpoints.

DSHO actuator achieved a payload of 134.571 N maximum, 216.248 times of its weight.

2) Actuator Lateral Stiffness Test: Fulfilled with water and connected to the atmosphere, a DSHO actuator was pulled laterally by a linear motion module at a constant velocity, while a force sensor was measuring the tension. The test result was recorded and shown in Fig. 6(g). The data was linearly fitted by a line with a slope of $k_{DSHO\_lateral} = 0.219$ N/mm.

B. Characteristics Test of the PBOC Joint

1) Joint Axial Characteristics Test: With the mechanism similar to the part with fixed lengths in IV-A1), the joint axial characteristics test was performed on the setup shown in Fig. 6(c), in which four DSHO actuators shared one pipeline. The result and fitting lines are shown in Fig. 6(f). The stiffness coefficient of the joint in the axial direction was calculated with the results of the equilibrium points of pressure with distinct ΔLs as $K_{joint\_axial} = 10.24$ N/mm, while the joint achieved a maximum force of 559 N, 91.119 times its weight (626 g in air).

2) Joint Lateral Characteristics Test: The lateral stiffness test shares the device used in IV.A.2) shown in Fig. 6(d). Four DSHO actuators shared one pipeline and were connected with the atmosphere. The test result is in Fig. 6(g), the lateral stiffness of the joint was calculated to be $k_{joint\_lateral} = 2.338$ N/mm by linear fitting. The test results in IV-A2). and this section show that the lateral stiffness gain $G_{lateral} = k_{joint\_lateral}/k_{DSHO\_lateral} = 10.67 > 4$. The lateral stiffness of the joint is amplified by a factor of 10.67, enhancing the resistance to lateral disturbances.

Futhermore, the lateral output force test was carried out with the force sensor fixed and modifications on the pipeline connections of actuators: the positive group and the negative one shared a water pipeline respectively (see in Fig. 6(d)). The internal pressure of P group was regulated to a fixed positive pressure (60 kPa), while that of N group was regulated to various negative pressures shown in Fig. 6(h). As shown in the figure, the joint's maximum lateral output force was 93.1 N.

C. The Depth-Compensation Free Actuation Test

As is shown in Fig. 7(d), we set up a minimum relative pressure regulator, consisting of a gear pump, two hydraulic solenoid valves, and a relative pressure sensor. A DSHO actuator was installed on a structure similar to that in IV-A1), with dual springs simulating a payload. The ambient hydraulic pressure at 10 m increments from 0 m to 60 m was simulated in the high-pressure water tank of the ocean depth simulator (YUEXIN, 0 m∼1000 m), and the regulator was operated by the control system through the signal wires externally (see in Fig. 7(a), (b), (c)). The tolerable depth of the regulator is limited by the potential closed cavities.

At each depth, the target relative pressure was set at 50 kPa to initiate actuation (see in Fig. 7(e1) and (e2)), while the relative pressures, achieved length, and ratio of length to pressure of the DSHO actuator were recorded and shown in Fig. 7(f) and (g).

The standard deviation of all ratio values is 0.0084 mm/kPa, therefore, the performance of the actuation and control system is consistent within 60 m depth.

D. Joint Forward Kinematics and Lateral Payload Test

1) Forward Kinematics Test: Experiment verificating the forward kinematics of the PBOC joint was implemented with the device in Fig. 8(a). The actuator pressures in the joint were manually regulated to a series of symmetric combinations, which resulted in theoretical endpoint positions in two symmetric planes of the joint (see in Fig. 8(b1)(c1)), while actual endpoint positions were measured with three laser displacement sensors. Procedures above were repeated with 1 kg payload installed on the top of the joint. The results and fitted curves under two distinct conditions are shown in Fig. 8(b2) (c2). It could be observed that the model deviation increases as the distance of the target point from the initial position increases, either with or without payload.

The position error of the measured points was calculated by $\|\boldsymbol{X}_{err}\| = \|\boldsymbol{X}_{measured}\| - \|\boldsymbol{X}_{ideal}\|$. The polynomial coefficients in the compensation function (6) were obtained by applying curve fitting with 2-order polynomial in X, Y, and Z axis direction respectively between $\boldsymbol{X}_{err}$ and $\boldsymbol{X}_{ideal}$:

$$[a_x, b_x, c_x] = [0.01, 1, 0], \qquad [a_y, b_y, c_y] = [0.005227, 1, 0],$$

$$[a_z, b_z, c_z] = \begin{cases} [-0.012743, 11.256808, -88.142427], z \geq 83, \\ [-0.001267, 1.210322, -9.084263], z < 83. \end{cases}$$

Endpoint position calculated with compensated model and the actual endpoint positions **without payload** are shown in Fig. 8(b3) and (c3) with mean average errors (MAE) in different areas, while Fig. 8(b4) and (c4) show those **with payload** installed. The MAE is defined as $MAE = (1/n)\sum_i^n |y_i - f(x_i)|$, where y_i is the i-th actual endpoint position i, $f(x_i)$ the i-th calculated endpoint position, and n the amount of test points. The results illustrated the high agreement between the test results of actively actuation and the calculated results by CCA-based kinematic model without payload. And it could be observed that the total MAE was enlarged after introducing a payload on the joint.

2) CCA Kinematic Model Compliance Test: In this test, the joint was passively deformed along the lateral direction by a suspending 2 kg mass (see in Fig. 8(d)). The endpoint pose $\{x, y, z, raw, pitch, yaw\}$ w.r.t. the initial one were measured with three laser displacement sensors and an IMU (CH100, HiPNUC) respectively in stasis.

P_1 and P_2 were the stable poses with and without the supporting plate respectively in Fig. 8(e), (f). P_1 was $(-5.3$ mm, 0 mm, 0.2 mm, $0°, -3.7°, 0°)$ with the supporting plate. Given the position component of P_1, the orientation calculated by the CCA-based kinematic model is $(-0.01°, -3.69°, 0.1°)$. P_2 was $(-7.3$ mm, 0 mm, 0.2 mm, $0.2°, -4.6°, 0°)$ without the supporting plate. The orientation of P_2 was calculated with model to be $(0.13°, -9.42°, -0.01°)$. The deviation ratio of model prediction is 0.27% with the supporting plate, nevertheless, without the supporting plate, the deviation ratio ended up being 51.16%. In consequence, it was proven to be effective for enhancing the compliance with CCA of the kinematic model of the joint to insert a supporting plate between end plates.

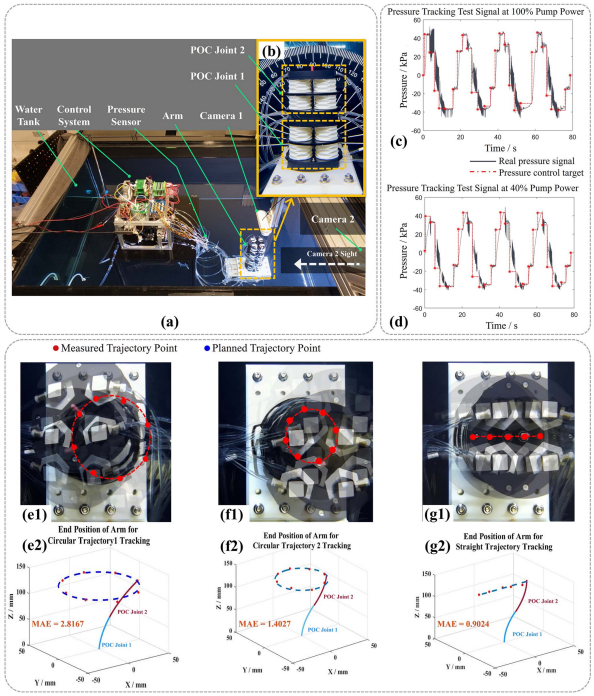

Fig. 9. (a) Trajectory tracking test device. (b) Manipulator detail. (c) and (d) Pressure tracking test signal at full and 40% pump power, respectively. The pressure oscillations in the regulation process were caused by solenoid valve operation and the hydraulic hammer effect. (e1) Circular trajectory 1; (f1) circular trajectory 2; (g1) straight trajectory in the view of camera 1 with measured points. And (e2) circular trajectory 1; (f2) circular trajectory 2 in camera 1; (g3) straight trajectory measured points and planned points.

E. Trajectory Tracking Test

In this section, with the flow control reducing the pressure oscillations, the endpoint trajectory tracking test was conducted with circular and linear paths to demonstrate the performance of the manipulator system. The experiment setup is shown in Fig. 9(a), in which the PBOC manipulator was fixed 80 cm underwater in the water tank, camera 1 fixed above the manipulator for top-view recording, and camera 2 fixed on the tank wall for side-view recording. The manipulator was constructed by connecting two PBOC joints in series (Fig. 9(b)), whose kinematic model was also derived for trajectory tracking.

With the pumps operating in full power, the consequence pressures from a sequence of target pressures were recorded and plotted in Fig. 9(c), which shows severe oscillations interferring feedback control due to hydraulic hammer effect, and then hindering the implementation of trajectory tracking. After reducing the pump power to 40%, the pressure oscillations exhibited a milder behavior, as shown in Fig. 9(d). To characterize the difference quantatively, the power sums of the base-frequency and harmonic components of oscillations in the frequency spectrum of pressure signals were calculated. The power sum with full pump power is 0.6853 W, while that with 40% pump power is 0.0446 W. Based on the signal analysis results, it could be claimed that the flow control in the FOC hydraulic actuation system could significantly reduce the power sum by 93.49% in pressure regulation, thus enhance the stability of subsequent trajectory tracking.

In order to simplify multi-solution problems in redundant soft manipulators, two joints were to commanded to perform the same motion or an opposite motion (see in Fig. 9(e2), (f2)).

Fig. 9(e1), (f1), (g1) show the trajectory tracking measurement results in the view of camera 1, while (e2), (f2), (g2) compare distinct target trajectories, measured trajectories, and MAEs respectively. It could be concluded that the manipulator system exhibited millimeter-level accuracy in the trajectory tracking test with the integration of adding support plate in the joint and FOC actuation system.

V. Conclusion and Future Work

In this work, a novel underwater manipulator system based on PBOC joints was proposed with outstanding payload capability, excellent structural stiffness, and accurate kinematic operations, effectively achieved through adding lateral supporting plates between the over-distant plates. The payload capability of a single proposed PBOC joint achieved a maximum linear output force 559 N without buckling, and a manipulator system weighs 5.83 kg with a load-to-weight ratio of 9.78. And the experiment results show that utilizing over-constrain design, the joint accords with CCA-based kinematic model well, with a sharply decreased prediction deviation (from 51.16% to 0.27%) under lateral payload compared to the one without over-constrain.

An FOC hydraulic actuation system with flow-controllable and depth-compensation free characteristics was developed, proved to work underwater with 60 m depth, and have reduced pressure oscillations by 93.49% in regulation with flow control, which could alleviate vibrations of the manipulator in trajectory tracking. Based on the developed kinematic models and semi-open-loop controller, the manipulator achieved accurate trajectory tracking in validation experiment. The summary of the performance of the proposed manipulator system is shown in Table II with the comparison with other manipulator systems. Besides the accuracy of the same order as typical SRH UW manipulators, this work performed a load-to-weight ratio one to two order of magnitude higher than the typical UW rigid manipulators.

Future work will focus on the multi-mode fused sensing to recognize the interaction with environment to improve control accuracy, and sequently achieve strategy-making with artificial intelligence. In addition, the depth limitation of the FOC system will be further extended to enable more accurate and dexterous operations at larger depths.

References

[1] A. Birk et al., "Dexterous underwater manipulation from onshore locations: Streamlining efficiencies for remotely operated underwater vehicles," *IEEE Robot. Automat. Mag.*, vol. 25, no. 4, pp. 24–33, Dec. 2018.

[2] Z. Shen et al., "An underwater robotic manipulator with soft bladders and compact depth-independent actuation," *Soft Robot.*, vol. 7, no. 5, pp. 535–549, 2020.

[3] B. Zhang et al., "An omnidirectional robotic platform with a vertically mounted manipulator for seabed operation," in *Proc. IEEE 17th Int. Conf. Automat. Sci. Eng.*, 2021, pp. 819–825. [Online]. Available: https://ieeexplore.ieee.org/document/9551420/

[4] D. R. Yoerger et al., "A hybrid underwater robot for multidisciplinary investigation of the ocean twilight zone," *Sci. Robot.*, vol. 6, no. 55, 2021, Art. no.eabe1901.

[5] O. Khatib et al., "Ocean one: A robotic avatar for oceanic discovery," *IEEE Robot. Automat. Mag.*, vol. 23, no. 4, pp. 20–29, Dec. 2016.

[6] I. Vasilescu et al., "AMOUR V: A hovering energy efficient underwater robot capable of dynamic payloads," *Int. J. Robot. Res.*, vol. 29, no. 5, pp. 547–570, 2010.

[7] J. J. Fernández et al., "Grasping for the seabed: Developing a new underwater robot arm for shallow-water intervention," *IEEE Robot. Automat. Mag.*, vol. 20, no. 4, pp. 121–130, Dec. 2013.

[8] B. Li, Y. Wang, K. Zhu, B. Chen, and H. Wu, "Structure design and control research of a novel underwater cable-driven manipulator for autonomous underwater vehicles," *Proc. Inst. Mech. Eng. Part M: J. Eng. Maritime Environ.*, vol. 234, no. 1, pp. 170–180, 2020. [Online]. Available: http://journals.sagepub.com/doi/10.1177/1475090219851948

[9] L. Chin, M. C. Yuen, J. Lipton, L. H. Trueba, R. Kramer-Bottiglio, and D. Rus, "A simple electric soft robotic gripper with high-deformation haptic feedback," in *Proc. IEEE Int. Conf. Robot. Automat.*, 2019, pp. 2765–2771.

[10] P. Polygerinos, Z. Wang, K. C. Galloway, R. J. Wood, and C. J. Walsh, "Soft robotic glove for combined assistance and at-home rehabilitation," *Robot. Auton. Syst.*, vol. 73, pp. 135–143, 2015.

[11] J. Shintake, V. Cacucciolo, D. Floreano, and H. Shea, "Soft robotic grippers," *Adv. Mater.*, vol. 30, no. 29, 2018, Art. no. 1707035.

[12] D. A. Ross, "Introduction to oceanography," 4th ed. Englewood Cliffs, NJ, USA: Prentice Hall, 1977.

[13] K. Ito, Y. Homma, and J. Rossiter, "The soft multi-legged robot inspired by octopus: Climbing various columnar objects," *Adv. Robot.*, vol. 34, no. 17, pp. 1096–1109, Sep. 2020. [Online]. Available: https://www.tandfonline.com/doi/full/10.1080/01691864.2020.1753570

[14] H. Zhong, Z. Shen, Y. Zhao, K. Tang, W. Wang, and Z. Wang, "A hybrid underwater manipulator system with intuitive muscle-level sEMG mapping control," *IEEE Robot. Automat. Lett.*, vol. 5, no. 2, pp. 3198–3205, Apr. 2020. [Online]. Available: https://ieeexplore.ieee.org/document/9001223/

[15] Z. Gong et al., "A soft manipulator for efficient delicate grasping in shallow water: Modeling, control, and real-world experiments," *Int. J. Robot. Res.*, vol. 40, no. 1, pp. 449–469, 2021.

[16] Q. Tan et al., "Underwater crawling robot with hydraulic soft actuators," *Front. Robot. AI*, vol. 8, 2021, Art. no. 688697.

[17] W. Zhu et al., "A soft-rigid hybrid gripper with lateral compliance and dexterous in-hand manipulation," *IEEE/ASME Trans. Mechatron.*, vol. 28, no. 1, pp. 104–115, Feb. 2023.

[18] B. T. Phillips et al., "A dexterous, glove-based teleoperable low-power soft robotic arm for delicate deep-sea biological exploration," *Sci. Rep.*, vol. 8, no. 1, pp. 1–9, 2018.

[19] L. Liu et al., "A bio-inspired soft-rigid hybrid actuator made of electroactive dielectric elastomers," *Appl. Mater. Today*, vol. 21, 2020, Art. no. 100814.

[20] X. Dong, Y. Wang, X.-J. Liu, and H. Zhao, "Development of modular multi-degree-of-freedom hybrid joints and robotic flexible legs via fluidic elastomer actuators," *Smart Mater. Struct.*, vol. 31, no. 3, Mar. 2022, Art. no. 035034. [Online]. Available: https://iopscience.iop.org/article/10.1088/1361-665X/ac5129

[21] J. Liu, X. Wang, S. Liu, J. Yi, X. Wang, and Z. Wang, "Vertebraic soft robotic joint design with twisting and antagonism," *IEEE Robot. Automat. Lett.*, vol. 7, no. 2, pp. 658–665, Apr. 2022.

[22] S. Tang et al., "Performance enhancement of the soft robotic segment for a trunk-like arm," *Front. Robot. AI*, vol. 10, Jul. 2023, Art. no. 1210217.

[23] L. Arleo, G. Stano, G. Percoco, and M. Cianchetti, "I-support soft arm for assistance tasks: A new manufacturing approach based on 3D printing and characterization," *Prog. in Additive Manuf.*, vol. 6, no. 2, pp. 243–256, May 2021. [Online]. Available: https://link.springer.com/10.1007/s40964-020-00158-y

[24] G. Olson, S. Chow, A. Nicolai, C. Branyan, G. Hollinger, and Y. Mengüç, "A generalizable equilibrium model for bending soft arms with longitudinal actuators," *Int. J. Robot. Res.*, vol. 40, no. 1, pp. 148–177, Jan. 2021.

[25] G. Olson, R. L. Hatton, J. A. Adams, and Y. Mengüç, "An Euler–Bernoulli beam model for soft robot arms bent through self-stress and external loads," *Int. J. Solids Struct.*, vol. 207, pp. 113–131, Dec. 2020.

[26] R. J. Webster III and B. A. Jones, "Design and kinematic modeling of constant curvature continuum robots: A review," *Int. J. Robot. Res.*, vol. 29, no. 13, pp. 1661–1683, 2010.

[27] Y. Guo, X. Chen, and Z. Wang, "Environmental insulation of 3D printable origamic soft actuators," in *Proc. IEEE 9th Annu. Int. Conf. CYBER Technol. Automat., Control, Intell. Syst.*, 2019, pp. 364–369.

[28] Y. Su et al., "A high-payload proprioceptive hybrid robotic gripper with soft origamic actuators," *IEEE Robot. Automat. Lett.*, vol. 5, no. 2, pp. 3003–3010, Apr. 2020.

[29] S. Liu et al., "A compact soft robotic wrist brace with origami actuators," *Front. Robot. AI*, vol. 8, 2021, Art. no. 614623.

[30] B. Jamil, G. Yoo, Y. Choi, and H. Rodrigue, "Hybrid robotic manipulator using sensorized articulated segment joints with soft inflatable rubber bellows," *IEEE Trans. Ind. Electron.*, vol. 69, no. 10, pp. 10259–10269, Oct. 2022. [Online]. Available: https://ieeexplore.ieee.org/document/9724119/